

Mass transfer dynamics in the dissolution of Taylor bubbles

Ghata M. Nirmal, Thomas F. Leary and Arun Ramachandran

I. CONCENTRATION GRADIENT IN THE BULK LIQUID SEGMENT

In the presence of a region of closed streamlines¹⁻³, one cannot invoke the simplifying assumption of representing the bulk liquid segment as a region with a uniform solute concentration; concentration gradients have to be accounted for in this region. This is incorporated in the proposed model by the transformation (see Eqs 4.2 - 4.12 in Rhines & Young²) of the unsteady state convective diffusive equation from a cylindrical coordinate system to a coordinate system comprised of time and the volume enclosed by a streamsurface (see Eq.2.13). Let $\psi = f(r)$ be the streamfunction for a set of nested, closed axisymmetric streamsurfaces in the cylindrical co-ordinates (see Fig. 1).

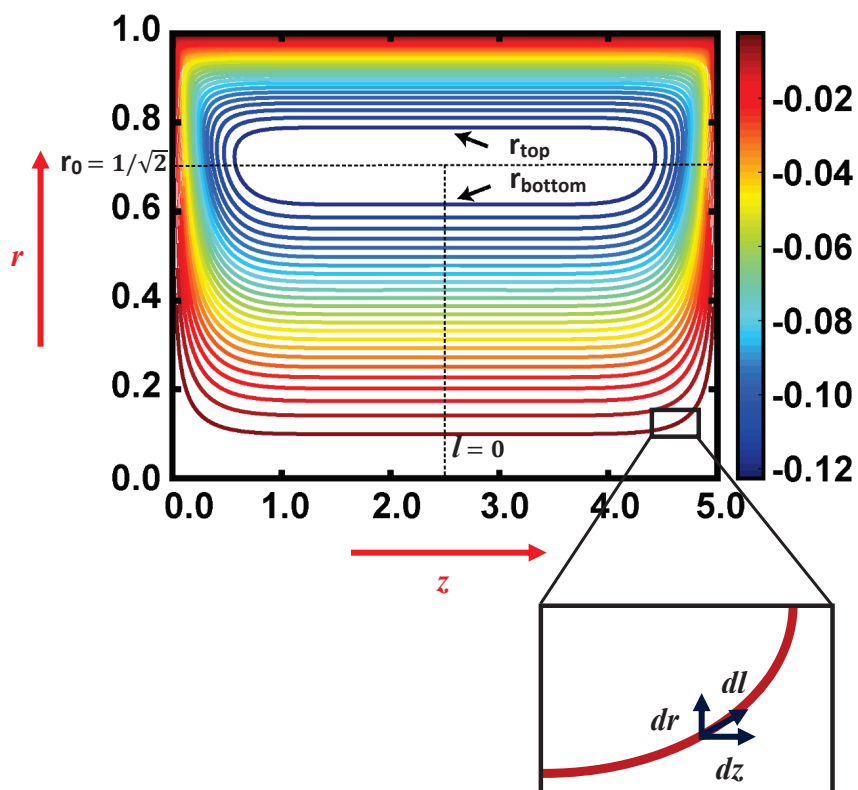


Figure 1. Streamline plot for the top half of the bulk liquid segment of length $\beta_L = 5$. The legend represents the values of the streamfunction ψ .

Consider the integral I of a scalar function $F(r, z, \theta)$, over a streamsurface, defined as,

$$I(\psi(r)) = \iiint_{V(\psi)} F(r, z, \theta) dV. \quad (\text{I.1})$$

Here, $F(r, z, \theta)$ is a scalar function, the volume refers to the volume enclosed by a particular streamsurface and r , z and θ are the radial, applicate and angular coordinates respectively. Following the approach of Rhines & Young², from Gauss Divergence Theorem,

$$\frac{dI}{d\psi} = \iint_{S(\psi)} \mathbf{n} \cdot \frac{\partial \mathbf{r}}{\partial \psi} F dS, \quad (\text{I.2})$$

where the normal \mathbf{n} is $\nabla\psi/|\nabla\psi|$, the differential area of a streamsurface $dS = 2\pi r dl$ and $|\nabla\psi| = rq$. The differential curvilinear co-ordinate, dl , is given by $\sqrt{(dr)^2 + (dz)^2}$ (see Fig.1) and q is the magnitude of the net velocity given by $\sqrt{u_r^2 + u_z^2}$. Thus, we can show that (using Green's Theorem),

$$\frac{dI}{d\psi} = 2\pi \oint_{L(\psi)} \frac{F}{q} dl, \quad (\text{I.3})$$

Here, $L(\psi)$ is the length of a streamline. Here, the axisymmetry of the geometry allows us to describe each streamsurface as a streamline. This derivation allows us to carry out the transformation by defining the average concentration across a streamsurface. Hence, the average concentration along a streamline is

$$\bar{C}_B(\psi) = \frac{\oint_{L(\psi)} C_B \frac{dl}{q}}{\oint_{L(\psi)} \frac{dl}{q}} = \frac{\oint_{L(\psi)} C_B \frac{dl}{q}}{T(\psi)}. \quad (\text{I.4})$$

Here, $T(\psi)$ is the circulation time, i.e., the time required for the solute to travel along the entire length ($L(\psi)$) of a streamline.

Substituting Eq.I.4 in the unsteady state convective diffusive equation,

$$\oint_{L(\psi)} \frac{\partial C_B}{\partial t} \frac{dl}{q} + \oint_{L(\psi)} q \frac{\partial C_B}{\partial l} \frac{dl}{q} = \mathcal{D} \oint_{L(\psi)} \nabla^2 C_B \frac{dl}{q}. \quad (\text{I.5})$$

The second term on the LHS is zero, since there is no variation in concentration along a

streamline in the limit of large Peclet numbers. The above equation then simplifies to

$$\begin{aligned}
 T(\psi) \frac{\partial \bar{C}_B}{\partial t} &= \mathcal{D} \oint_{L(\psi)} \nabla^2 C_B \frac{dl}{q} \\
 &= \frac{\mathcal{D}}{2\pi} \frac{\partial}{\partial \psi} \left[\iiint_{V(\psi)} \nabla^2 C_B dV \right] \\
 &= \frac{\mathcal{D}}{2\pi} \frac{\partial}{\partial \psi} \iint_{S(\psi)} \nabla \bar{C}_B \cdot \mathbf{n} dS \\
 &\quad \text{(From Gauss Divergence Theorem)} \\
 &= \frac{\mathcal{D}}{2\pi} \frac{\partial}{\partial \psi} \iint_{S(\psi)} \frac{\partial \bar{C}_B}{\partial \psi} \nabla \psi \cdot \mathbf{n} dS \\
 &= \frac{\mathcal{D}}{2\pi} \frac{\partial}{\partial \psi} \oint_{L(\psi)} \frac{\partial \bar{C}_B}{\partial \psi} 2\pi r^2 q dl
 \end{aligned} \tag{I.6}$$

Here we can substitute for $\frac{\partial \bar{C}_B}{\partial \psi}$ as a function of volume enclosed by a streamsurface (V),

$$\frac{\partial \bar{C}_B}{\partial \psi} = \frac{\partial \bar{C}_B}{\partial V} \frac{\partial V}{\partial \psi} = \frac{\partial \bar{C}_B}{\partial V} 2\pi T(\psi) \tag{I.7}$$

Therefore, from Eqs.I.6 and I.7,

$$\frac{\partial \bar{C}_B}{\partial t} = \frac{\partial}{\partial V} \left[\pi^2 \mathcal{D} \hat{\mathcal{D}}(\psi) \frac{\partial \bar{C}_B}{\partial V} \right] \tag{2.13}$$

The transformation to Eq.2.13 introduces a modified diffusivity, $\hat{\mathcal{D}}$, defined as,

$$\hat{\mathcal{D}}(\psi) = 4\omega(\psi)T(\psi). \tag{I.8}$$

Here, $\omega(\psi)$ is the circulation along a streamline given by

$$\omega(\psi) = \oint_{L(\psi)} r^2 q dl. \tag{I.9}$$

$\hat{\mathcal{D}}$ can be determined for varying liquid segment lengths using the exact velocity distribution from the analytical solution⁴ at each instant of time, but this can be computationally expensive. To reduce this cost, we propose a semi-empirical correlation for $\hat{\mathcal{D}}$ as a function of β_L using our understanding of the flow physics. The fluid velocity in the radial direction (u_r) drops to 0 within a distance of R from the bubble caps. The fluid velocity in the applied direction (u_z), rendered dimensionless with respect to the bubble velocity U_B , is fully developed after this length scale (R) and is given by

$$u_z = 1 - 2r^2. \tag{I.10}$$

For long liquid segment lengths ($\beta_L \gg 1$), the contribution to ω and T can be, hence, attributed only to flow in the applicate direction. Using this approximation, the circulation given by Eq.I.9 is simplified to

$$\omega(\psi) = \beta_L(r_{top}^2|1 - 2r_{top}^2| + r_{bot}^2|1 - 2r_{bot}^2|). \quad (\text{I.11})$$

Here, r_{top} and r_{bot} are the radii that correspond to a particular streamline ψ (see Fig.1). These are given by the roots of the following equation,

$$\psi = \frac{1}{2}(r^4 - r^2). \quad (\text{I.12})$$

In the inner regions of the vortex, the circulation time diverges as u_z drops to 0 at $r_0 = \frac{1}{\sqrt{2}}$. Here, the streamfunction reaches its maximum magnitude, $|\psi_{max}| = 1/8$. A linear perturbation around r_0 assists us in determining the exact nature of this singularity. Let ε be a small parameter defined as $\varepsilon = r - r_0$. From Eq.I.10,

$$u_z = u_z^{(0)} + \varepsilon u_z^{(1)} = 1 - 2r_0^2 + \varepsilon(-4r_0) + O(\varepsilon^2) = \varepsilon(-4r_0). \quad (\text{I.13})$$

Also, from Eq.I.12 the streamfunction is given by,

$$\begin{aligned} \psi &= \psi^{(0)} + \varepsilon\psi^{(1)} + \varepsilon^2\psi^{(2)} \\ &= \frac{1}{2} [(r_0^4 - r_0^2) + \varepsilon(2r_0^3 - r_0) + \varepsilon^2(6r_0^2 - 1)] + O(\varepsilon^4) \\ &= \psi_{max} + \varepsilon^2. \end{aligned} \quad (\text{I.14})$$

From Eq.I.14,

$$\varepsilon = \sqrt{\psi - \psi_{max}}. \quad (\text{I.15})$$

From Eqs.I.13 and I.15, we propose an expression to describe the circulation time. Since the liquid segments are long, we can ignore the circulation time arising from the radial components and the circulation time is well described in this limit by,

$$T = L(\psi)/u_z = 2\beta_L/((-4r_0\varepsilon)|) = \frac{a\beta_L}{\sqrt{\psi - \psi_{max}}}. \quad (\text{I.16})$$

In the above equation, a is a constant that depends on β_L .

In the outer regions of the vortex, as one approaches the bubble cap, the presence of a stagnation point⁵ gives rise to a logarithmic singularity⁶. Therefore, for the outer streamlines,

$$T = b_1 \log(\psi) + b_2. \quad (\text{I.17})$$

From Eqs.I.16 and I.17, we propose the following expression for T ,

$$T = \frac{a\beta_L}{\sqrt{\psi_{max} - \psi}} + b_1 \log(\psi) + b_2. \quad (\text{I.18})$$

The fitting parameters a , b_1 and b_2 are the estimated by comparing Eq.I.18 to the numerically predicted circulation time for different liquid segment lengths. While $b_1 = -1.95 \pm 0.08$ and $b_2 = 2.81 \pm 0.25$ are independent of β_L , a portrays the following functionality,

$$a = 0.66 - 0.4e^{-0.11\beta_L}. \quad (\text{I.19})$$

\hat{D} can be now determined, using Eqs.I.8,I.11 and I.18, for a given liquid segment length. These numerical predictions were carried out in MATLAB 2017a. A gaussian mesh was generated in the radial as well as applicate direction (to avoid erroneous results near the stagnation point) with a maximum step size of 0.002. The velocity profile and the stream-function were computed at these node points and the *contour* function was used to generate the closed streamline contours for each value of ψ . $T(\psi)$ (see Eq.I.18), $V(\psi) = \oint \pi r^2 u_r dl$ and $\omega(\psi)$ (see Eq.I.11) were computed for each contour using spline integration to subsequently calculate $\hat{D}(\psi)$ using Eq.I.8. Fig.2 compares the numerical result of $\hat{D}(\psi)$ to that predicted by the proposed correlation for $\beta_L = 20$.

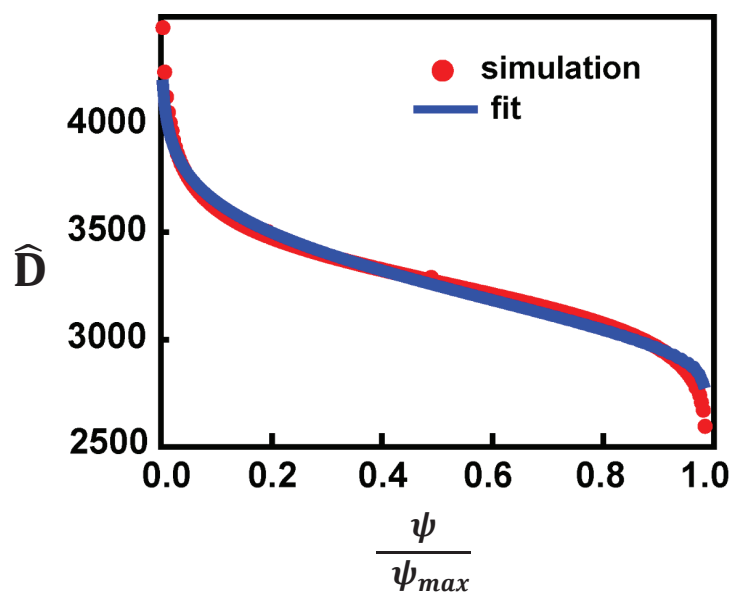


Figure 2. Comparison of numerically predicted \hat{D} to a proposed correlation (Eqns.I.8,I.11 and I.18) for $\beta_L = 20$

II. INITIAL CONCENTRATION DISTRIBUTION

This section describes the setup and execution of the two-dimensional, laminar flow, two-phase flow simulation carried out in COMSOL Multiphysics[®] 5.3a. Results from this simulation enabled us to describe the initial dissolved gas concentration in the bulk liquid segment after pinch-off at the T-junction. The simulation was carried out in two steps. First, the laminar, two-phase flow through a T-junction microchannel (width 100 μm) was modeled using the Level Set method. The inlet flow rates of carbon dioxide and ethanol were fixed at 300 $\mu\text{L/s}$ and 500 $\mu\text{L/s}$ respectively. The pressure was set to 0 at the outlet and backflow was suppressed. A direct(PARDISO), time-dependent solver was used to solve for the velocity and the level set variable, ϕ . $\phi = 1$ corresponds to the pure carbon dioxide phase and $\phi = 0$ corresponds to the ethanol phase. Next, results from the first step were used to track dissolved gas concentration, c , during bubble formation by numerically integrating the following partial differential equation,

$$(1 - \phi)\frac{\partial c}{\partial t} + \nabla \cdot (-(1 - \phi)\mathcal{D}\nabla c) + (1 - \phi)\mathbf{u} \cdot \nabla c + \phi c = \phi. \quad (\text{II.1})$$

Here, \mathbf{u} is the velocity field. On substituting $\phi = 0$ in Eq.II.1, we recover the unsteady state convection diffusion equation to describe the dissolved gas concentration in the liquid phase. On the other hand, $\phi = 1$ corresponds to the gas phase. This step used a direct(PARDISO), time-dependent solver and required adaptive mesh refinement to minimize error. Results from this simulation are summarized in Fig.2(a) and (b). Although these results give a qualitative sense of the distribution of the dissolved gas, it is not possible to repeat these simulations for every experiment owing to high computational cost. Therefore, an additional set of simulations was carried out using COMSOL Multiphysics[®] 5.3a for one unit cell to investigate the evolution of the dissolved gas concentration profile in the liquid segment. In this case, a moving wall boundary condition (at velocity $-U_B$) was applied to the capillary wall and laminar flow was imposed. A direct(PARDISO), stationary solver was used to evaluate the steady state velocity profile. Next, an unsteady state convection diffusion equation was solved for a given Pe using the velocity profile obtained from the first step. Here, the liquid segment continuously received solute from the bubble caps and a non-uniform and asymmetric concentration was imposed as the initial condition (see Fig.2 (c)). A direct(PARDISO), time-dependent solver was used to track the dissolved gas concentration.

Results from this study are summarized in Fig.2(c).

III. NUMERICAL METHOD

The governing equations listed in section 2.1 for each of the regions in a unit cell were used to predict the dynamic bubble lengths as a function of distance traveled in the capillary for a given solubility, β_L , initial β_B and the steady state Pe and Ca (i.e., when the bubble stops dissolving). In-house MATLAB scripts were used to carry out the integration (using ode15s) for the following set of ordinary differential equations for each unit cell:

For the bubble volume:

1.

$$\frac{d\rho_G V_{B,i}}{dt} = -k_{L,i} A_{B,i} (C_{sat} - C_{B,i}) - k_{L,i} A_{B,i} (C_{sat} - C_{B,i+1}) - 2\pi U_{B,i} R_{B,i} \delta_i (\bar{C}_{BF,i} - \bar{C}_{LF,i}). \quad (2.18)$$

For the distance traveled by the i^{th} bubble:

2.

$$\frac{dX_i}{dt} = U_{B,i} \quad (III.1)$$

For dissolved gas concentration in the i^{th} liquid segment, a set of ODEs corresponding to the grid of streamfunction values was integrated owing to the coordinate transformation conducted in section 2.1.2 (see Eq.2.13). The central difference method was used to discretize the dimensionless BLS volume (into smaller volumes ΔV) using 201 nodes (or streamlines). Therefore, for j^{th} streamline in the i^{th} unit cell, the differential equation for the average dissolved gas concentration is given by:

3.

$$\frac{\partial \bar{C}_{B,i}}{\partial t} = \pi^2 \frac{\partial}{\partial V} \left[\mathcal{D} \hat{\mathcal{D}}(\psi) \frac{\partial \bar{C}_{B,i}}{\partial V} \right], \quad (2.13)$$

which can be discretized to give:

$$\frac{d\bar{C}_{B,i}(\psi_j)}{dt} = \pi^2 \frac{\mathcal{D} \hat{\mathcal{D}}_{j+1} \frac{\bar{C}_{B,i}(\psi_{j+2}) - \bar{C}_{B,i}(\psi_j)}{2\Delta V} - \mathcal{D} \hat{\mathcal{D}}_{j-1} \frac{\bar{C}_{B,i}(\psi_j) - \bar{C}_{B,i}(\psi_{j-2})}{2\Delta V}}{2\Delta V} \quad (III.2)$$

The boundary conditions, Eqs.2.14 and 2.15, were also discretized in a similar manner to define the ODEs for the outermost and innermost streamline. For each of these streamlines, \hat{D} was calculated using Eqs.I.8,I.11 and I.18. This integration was carried out for 10 unit cells (therefore, atleast 203×10 ODEs) on an average to ensure periodicity in the gas bubble lengths and dissolved gas concentration. The number of unit cells had to be increased to a maximum of 35 for simulations involving high Pe and high Ca. The bubbles were introduced periodically into the capillary, and the initial bubble length was defined such that it starts dissolving only after pinch off. To take the dissolution during bubble formation into account, each BLS contained a finite amount of dissolved gas whose profile (as a function of streamfunction) was given by Eq.2.17. The BF and LF concentrations were computed at each timestep using Eqs.2.6 and 2.10, respectively. After each integration step, the velocities for each bubble in the frame of reference of the leading bubble was solved by finding the root of Eq.2.19. This information was used to dynamically update Pe_i , Ca_i (hence δ_i), $\beta_{B,i}$, $k_{L,i}$ and $R_{B,i}$.

Fig.4 investigates the effect of the three major limitations of prior models in the literature on the diffusivity predictions. To ignore cross-talk, $\overline{C}_{BF,i}$ and $\overline{C}_{LF,i}$ were fixed to be C_{sat} for every unit cell to ensure no mass transfer to and from the BF and the LF regions. To disregard the concentration inhomogeneity, Eq.2.11 was used (instead of Eq.2.13) to compute the average dissolved gas concentration in the BLS at each time step. Finally, to ignore the change in bubble velocities, velocity of every bubble was set to be equal to the average velocity. This average velocity was obtained by averaging the bubble velocity measured from experiments over the distance that it underwent 95% of the total shrinkage. For the comprehensive model that takes all the limitations into account, the numerical predictions were carried out on the basis of the leading bubble's velocity, i.e., the velocity attained by a bubble once it stops shrinking (steady state achieved). The bubble velocity at the entrance (at the point of pinch off) was then computed based on the shrinkage rates of the bubble at the entrance and all the preceding bubbles. This computation step was faster for slowly dissolving bubbles as opposed to those dissolving rapidly. Moreover, less number of unit cells (10 as opposed to 35) were suffice for slowly dissolving bubbles, leading to an additional reduction in the computational load. Hence, the authors recommend the experimentalists to tune the operational parameters such that the dissolution is not too rapid. The authors

are willing to share the MATLAB scripts upon request with researchers interested in using the platform for solubility and diffusivity measurements.

IV. EXPERIMENTAL DETAILS

This section summarizes the experimental conditions and the fitting parameters obtained from the experimental data sets. The experimental protocol is outlined in section 3.1. Fig. 3 shows the variation of normalized bubble length with dimensionless distance for (a) ethanol and (b) silicone oil. The normalized bubble length is defined as $(\beta_B - \beta_{B,s}) / (\beta_{B,in} - \beta_{B,s})$, where $\beta_{B,in}$ is the dimensionless bubble length right after pinch-off and $\beta_{B,s}$ is the steady state dimensionless bubble length (i.e., once the bubble stops dissolving).

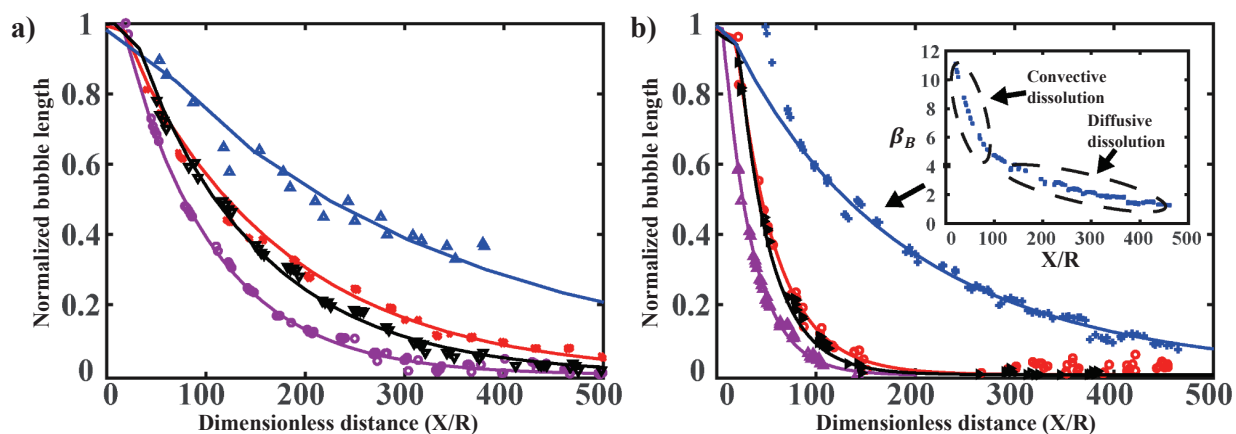


Figure 3. (a) shows the normalized bubble length as a function of dimensionless distance (dimensionless with respect to R) for CO_2 dissolution in ethanol under different conditions: $P_{g,in} = 3$ psig and $P_{l,in} = 4$ psig (\blacktriangle); $P_{g,in} = 1$ psig and $P_{l,in} = 2$ psig (\times); $P_{g,in} = 2$ psig and $P_{l,in} = 3.5$ psig (\blacktriangledown); $P_{g,in} = 1.7$ psig and $P_{l,in} = 3.2$ psig (\circ). (b) shows the normalized bubble length as a function of dimensionless distance for CO_2 dissolution in silicone oil under different conditions: $P_{g,in} = 5.23$ psig and $P_{l,in} = 3.58$ psig ($+$); $P_{g,in} = 3.72$ psig and $P_{l,in} = 5.35$ psig (\circ); $P_{g,in} = 3.15$ psig and $P_{l,in} = 4.34$ psig (\blacktriangleright); $P_{g,in} = 3.19$ psig and $P_{l,in} = 4.38$ psig (\blacktriangleleft). The solid lines in (a) and (b) correspond to their respective fits using the proposed model. $P_{g,in}$ and $P_{l,in}$ are inlet gauge pressure values of the gas and the liquid respectively. The maximum value of the sum of residuals for the fits was 0.071. See Table I for more details.

The numerical method for fitting is outlined in ESI III. Across the experimental data sets, the variability in the fitted diffusion coefficients and the fitted Henry’s constant do not exceed 4.8% and 3.38%, respectively. The fitting parameters across each experimental data set are accurate up to 0.7%.

The bubble dissolution process is highly dynamic in nature; the literature reports that up to 10% mass transfer can occur during the bubble formation stage⁷. To avoid fitting for a fictitious initial bubble length, we have fit for the initial concentration distribution (see Eq.2.17) at the point of bubble pinch-off, and regarded that bubble length as the initial bubble length. The purpose of including the inset in Fig. 3 (b) is to highlight the two regimes of bubble dissolution in Taylor flow. This has never been experimentally reported in the literature, although it has been recently acknowledged⁸ via volume-of-fluid based simulations. The first regime is convection-controlled dissolution and is characterized by the initial sharp decrease in the bubble length. This is when the initial period where BLS first receives gas and homogenizes it along contours of constant ψ . The second regime is diffusion-controlled dissolution and is depicted by the slower decrease in the bubble length during later time. Observation of the two separate regimes was made possible due to choice of a viscous liquid (such as silicone oil), hence lower Pe. Although this regimes exist in ethanol as well, the time scale over which the dissolution is convection-controlled is small as compared to the bubble formation time (higher Pe), and cannot be recorded in our experiments. Recall that our proposed model assumes that dissolved gas concentration is homogeneous along a particular streamsurface. Hence, to deal with this shortcoming, we fit for the experimental data that lies only in the second (diffusion-controlled) regime. The fitting parameters and dimensionless parameters for each of these curves are summarized in table I.

In table I, Pe_{in} and Ca_{in} are the initial Pe and Ca respectively (i.e., right after bubble pinch-off). Pe_s and Ca_s are the steady state Pe and Ca respectively (i.e., once the bubble stops dissolving). These are different due to decrease in the bubble velocity upon dissolution, which can be as high as 32%. $O(\chi)$ states the order of χ . Unlike the popular assumption in the literature, for most experiments, the liquid film’s contribution to mass transfer is as important as the bubble caps. Even in the one case when $O(\chi) \sim 0.1$, the liquid film’s contribution to mass transfer cannot be ignored at short time scales. This is due to high concentration gradients in a solute-devoid BLS during the initial dissolution stage.

Table I. Experimental parameters

Legend (in Fig. 3)	$P_{g,in}$ (psig)	$P_{l,in}$ (psig)	Pe_{in}	Ca_{in}	$\beta_{B,in}$	Pe_s	Ca_s	$\beta_{B,s}$	β_L	Regime	$O(\chi)$	Fitting parameters			
<i>Ethanol</i>												$D \times 10^9$ (m ² /s)	C_{out}	t_0^*	
▲	3.00	4.00	7450	0.0150	25	6940	0.0140	22	4	4	1	3.89	1.00	0.02	
✕	1.00	2.00	526	0.0011	12	356	0.0007	5	10	1	0.1	3.63	0.73	0.02	
▼	2.00	3.50	2760	0.0049	20	2700	0.0048	15	6	1	1	3.55	1.00	0.02	
○	1.70	3.20	2040	0.0041	17	1350	0.0027	8	9	1	1	3.92	0.45	24.5	
<i>Silicone Oil</i>												$D \times 10^9$ (m ² /s)	C_{out}	t_0^*	K_H (atm)
+	3.58	5.23	195	0.0187	12	146	0.0140	1	32	1	1	3.08	0.86	2.24	294
○	3.72	5.35	509	0.0433	16	482	0.0410	12	16	1	1	2.90	0.87	0.16	294
▶	3.15	4.34	369	0.0323	19	343	0.0300	13	12	1	1	2.84	0.42	0.94	310
▲	3.19	4.38	211	0.0181	6	198	0.0170	4	13	1	1	2.84	0.85	2.04	284

V. REGIMES OF MASS TRANSFER IN DISSOLVING TAYLOR BUBBLES

This section outlines four regimes of operation encountered in dissolving Taylor bubbles. The regime map has been established based on a scaling analysis that depends on four dimensionless parameters, the Péclet number, $Pe = U_B R / \mathcal{D}$, the liquid film thickness, δ , the dimensionless liquid length, $\beta_L = L_L / R$ and the dimensionless bubble length, $\beta_B = L_B / R$. Here, U_B is the bubble velocity, R is the radius of the tube, \mathcal{D} is the gas diffusivity in liquid, μ is the liquid viscosity, γ is the interfacial tension, L_L is the liquid segment length and L_B is the gas plug length. Depending on the operating conditions, either the bubble caps or the liquid film (of thickness δ) can play a dominating role in delivering gas to the bulk liquid segment. δ is a function of the Capillary number, $Ca = U_B \mu / \gamma$ (see Eq.2.5). As described in section 4, depending on the liquid film thickness and concentration boundary layers originating from the bubble and the film regions, there exist four possibilities during the dissolution process.

First, consider the case when the liquid film surrounding the bubble is saturated with gas. For this assumption to be justified, the diffusion time scale over δ should be less than the convective time scale of the liquid film to traverse the bubble length,

$$\frac{\delta^2}{\mathcal{D}} \ll \frac{L_B}{U_B}. \quad (\text{V.1})$$

This simply means that the thickness of the concentration boundary layer surrounding BF ($\delta_B \sim \sqrt{(L_B \mathcal{D} / U_B)}$) exceeds the film thickness, i.e.,

$$\delta \ll \delta_B. \quad (\text{V.2})$$

From the Eq. V.1, the condition for saturation of the liquid film (BF) surrounding the bubble (see R-1 and R-2 in Fig.5),

$$\text{Pe}\delta^2 \ll \beta_B \text{ or } \frac{\text{Pe}\delta^2}{\beta_B} \ll 1. \quad (\text{V.3})$$

The amount of solute transferred from this saturated liquid film once it contacts the liquid segment is

$$N_{F-L} = k_L|_{F-L}(C_{sat} - C_B)2\pi R_B L_L. \quad (\text{V.4})$$

Here, C_B is the concentration of solute in the bulk liquid segment and C_{sat} is the saturation concentration. The LF-to-BLS volumetric mass transfer coefficient, $k_L|_{F-L}$, can be described as

$$k_L|_{F-L} \sim \frac{\mathcal{D}}{\delta_L}, \text{ where} \quad (\text{V.5})$$

$$\delta_L \sim \sqrt{\frac{\mathcal{D}R_B}{U_B}} \quad (\text{V.6})$$

Here, δ_L is the concentration boundary layer thickness developed in the LF region. The above scaling is valid for the limit (see R-2 in Fig.5), $\delta_L \ll \delta$ or $\frac{\text{Pe}\delta^2}{\beta_L} \gg 1$. In similar vein, the amount of solute transferred from the bubble caps to the liquid segment is:

$$N_{BC-L} = k_L|_{BC-L}(C_{sat} - C_B)2\pi R_B^2. \quad (\text{V.7})$$

The bubble caps-to-liquid volumetric mass transfer coefficient, $k_L|_{BC-L}$, can be described as

$$k_L|_{BC-L} \sim \frac{\mathcal{D}}{\delta_{BC}}. \quad (\text{V.8})$$

Here, δ_{BC} is the concentration boundary layer thickness developed around the bubble caps defined as

$$\delta_{BC} \sim \sqrt{\frac{\mathcal{D}R_B}{U_B}}. \quad (\text{V.9})$$

The ratio of the amount of gas received from liquid film to that from the caps is

$$\chi = \frac{N_{F-L}}{N_{BC-L}}. \quad (\text{V.10})$$

From Eqs. V.4, V.5, V.6, V.7, V.8 and V.9,

$$\chi = \sqrt{\frac{L_L}{R}} = \sqrt{\beta_L}. \quad (\text{V.11})$$

Second, in the limit (see R-1 in Fig.5), $\delta \ll \delta_L$, or $\frac{Pe\delta^2}{\beta_L} \ll 1$, χ can be deduced to be,

$$\chi = \delta\sqrt{Pe}. \quad (V.12)$$

Third, in the limit when the liquid film is only partially saturated (R-3 and R-4 in Fig.5), or

$$\frac{Pe\delta^2}{\beta_B} \gg 1, \quad (V.13)$$

the driving force for mass transfer from the liquid film to the liquid segment is reduced. Assuming that the liquid segment is initially devoid of the gas, the ratio χ for the limit $\delta_L \ll \delta$ (R-4 in Fig.5), is

$$\chi = \frac{1}{\delta} \sqrt{\frac{\beta_L\beta_B}{Pe}}. \quad (V.14)$$

Fourth, in the limit $\delta \ll \delta_L$ (R-3 in Fig.5),

$$\chi = \sqrt{\beta_B}. \quad (V.15)$$

Therefore, we can predict χ for all four possible cases (see Fig.5).

VI. THEORETICAL VALIDATION OF THE PROPOSED MODEL

Muradoglu et. al⁹ used a finite volume/ front-tracking method (two-dimensional geometry) to investigate axial dispersion of a solute injected in the leading liquid segment in a train of non-dissolving bubbles. The authors studied the effect of varying capillary number and Péclet number on axial dispersion. To validate our proposed model, we have introduced a passive solute in the leading liquid segment ($n=0$ in Fig.4 (a)) in a train of six non-dissolving bubbles. Fig.4 (a) compares the numerical predictions from this work with that from Muradoglu et. al⁹ in the convection-controlled limit ($Pe = 100$ and $Ca=0.01$). There is a reasonably good agreement in the average tracer concentration profiles in the liquid segments. A slight disagreement is observed when the subsequent liquid segments initially receive the solute (see $n = 2, 3$ and 4 in Fig.4 (a)). This is because, for low Pe , it takes the solute a finite amount of time to circulate along a streamline. However, our proposed model assumes homogenous concentration along every streamline at a given time. This is a fair assumption for the intended application of this model, since such experiments entail $Pe \gg 1$. Fig.4 (b) compares the average tracer concentration profiles at various dimensionless times,

\hat{t} , (dimensionless with respect to the convective time scale) with the results from Muradoglu et. al⁹ and the theoretical expression proposed by Pederson and Horvath¹⁰.

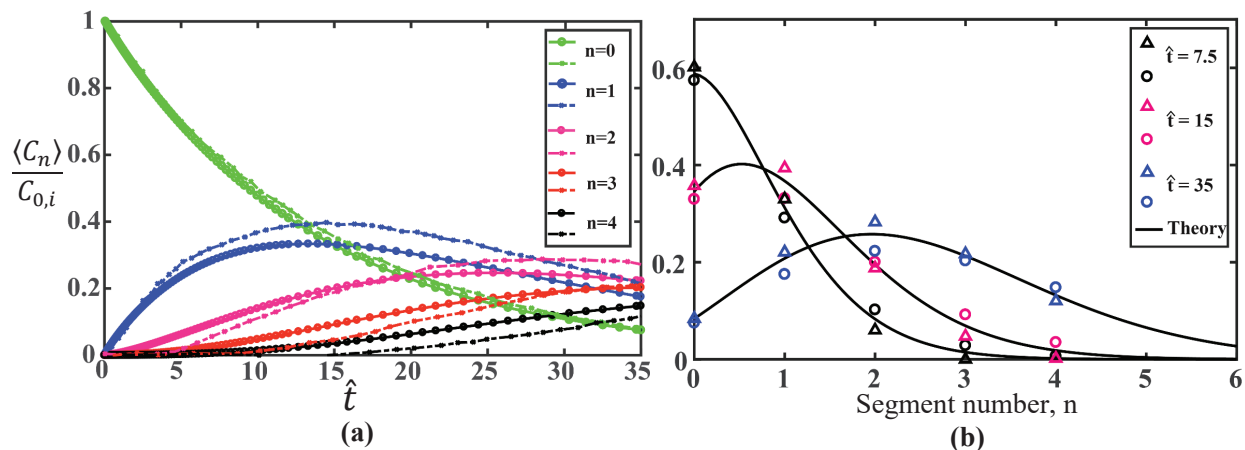


Figure 4. (a) shows the average solute concentration profiles in the bulk liquid segments in a train of six non-dissolving bubbles for $\beta_L = 0.75$ at $Pe= 100$ and $Ca= 0.01$. The hollow circles with the solid line correspond to this work and dash-dotted line with ‘x’ marker correspond to Muradoglu et. al⁹. (b) compares the same results to theoretical predictions of Pederson and Horvath¹⁰ (solid black line) given by the Poisson distribution. Here the hollow circles are results from this work and hollow triangles are predictions of Muradoglu et. al⁹.

We were unable to compare the results in the diffusion-controlled limit ($Pe=10^4$) because Muradoglu et. al⁹ provides the results only up to $\hat{t} \sim 35$. Such time-scales are not physically captured in the simulations, and are much shorter than the experimental time scales over which bubble dissolution is observed, since the latter are controlled by diffusion.

REFERENCES

- ¹A. Acrivos, *Journal of Fluid Mechanics*, 1971, **46**, 233–240.
- ²P. B. Rhines and W. R. Young, *J. Fluid Mech.*, 1983, **133**, 133–145.
- ³W. Young, A. Pumir and Y. Pomeau, *POFA*, 1989, **1**, 462–469.
- ⁴J. L. Duda and J. S. Vrentas, *Journal of Fluid Mechanics*, 1971, **45**, 247.
- ⁵G. I. Taylor, *Journal of Fluid Mechanics*, 1960, **9**, 218.
- ⁶H. Winter, C. Macosko and K. Bennett, *Rheologica Acta*, 1979, **18**, 323–334.

- ⁷C. Yao, Z. Dong, Y. Zhao and G. Chen, *Chemical Engineering Science*, 2014, **112**, 15–24.
- ⁸L. Yang, M. J. Nieves-Remacha and K. F. Jensen, *Chemical Engineering Science*, 2017, **169**, 106–116.
- ⁹M. Muradoglu, A. Günther and H. A. Stone, *Physics of Fluids*, 2007, **19**, 1–11.
- ¹⁰H. Pedersen and C. Horvath, *Industrial and Engineering Chemistry Fundamentals*, 1981, **20**, 181–186.